Linear Stability Analysis of Time-Averaged Flow Past a Cylinder

Sanjay Mittal[1]

Abstract: Flow past a circular cylinder looses stability at a Reynolds number, $Re \sim 47$. It has been shown, in the past, that the linear stability analysis (LSA) of the steady state solution can predict not only the critical Re, but also the non-dimensional frequency, St, of the associated instability. For larger Re the non-linear effects become important and the LSA of the steady-state flow does not predict the correct St. It is shown that, in general, the LSA applied to the time-averaged flow can result in useful information regarding its stability. This idea is applied to the $Re = 100$ flow past a circular cylinder. The LSA of the time-averaged flow results in the correct value of St. Proper Orthogonal (POD) or Karhunen-Loéve (K-L) decomposition of the unsteady flow using the snapshot method is also carried out. The modes from this decomposition are compared to the unstable modes computed using the LSA.

Keyword: Circular Cylinder, Linear Stability Analysis, Finite Element Method, Reynolds Averaged Navier Stokes Equations, Proper Orthogonal Decomposition, Karhunen-Loéve (K-L) decomposition.

1 Introduction

The steady flow past a circular cylinder becomes unstable beyond $Re \sim 47$ and eventually leads to von Karman vortex shedding (Williamson (1996)). Various investigations, in the past, have shown that the Linear Stability Analysis (LSA) of the steady-state flow can provide a reasonably accurate estimate of the critical Reynolds number (Re_c) and the non-dimensional vortex shedding frequency (St_c) at the onset of the instabil-

ity (Jackson (1987); Morzynski, Afanasiev, and Thiele (1999); Ding and Kawahara (1999); Mittal and Kumar (2003); Kumar and Mittal (2006)). In a recent study (Kumar and Mittal (2006)) it has been shown, via the LSA analysis, that to a large extent the blockage can explain the scatter in the data for the critical parameters at the onset of the instability, from various researchers in the past. The extrapolated values for a computational domain with infinite lateral width are $Re_c = 47.380$ and $St_c = 0.1163$.

For Re beyond Re_c, the non-linear terms become increasingly important and the LSA of the steady-state flow ceases to provide any useful information. For example, the St predicted by the LSA of the stationary solution for $Re = 100$ is much lower than the value observed via experiments and direct time integration of the governing equations. In addition, it becomes increasingly difficult to generate a steady-state solution for higher Re. Mittal (2008) has shown that linear stability analysis of the time-averaged flows can lead to useful information. In this paper we investigate the possibility of generating useful information, especially for the St, from the linear stability analysis of the time-averaged flow past a circular cylinder.

The Proper Orthogonal (POD) or Karhunen-Loéve (K-L) decomposition of unsteady flows using the snapshot method has been used in the past for extracting the most relevant spatial structures for constructing a low-dimensional flow model (Sirovich (1987); Noack, Afanasiev, Morzynski, Tadmor, and Thiele (2003); Hasan and Sanghi (2007)). The K-L decomposition for the $Re = 100$ unsteady flow past a cylinder is carried out in this work. The modes are compared to the unstable modes predicted by LSA.

A stabilized finite element formulation is

[1] Department of Aerospace Engineering, Indian Institute of Technology Kanpur, UP 208 016, India. Email: smittal@iitk.ac.in; Phone: +91 512 2597906; Fax: +91 512 2597561.

used that allows one to employ equal-order-interpolation functions for velocity and pressure. The SUPG (Streamline-Upwind/Petrov-Galerkin) and PSPG (Pressure-Stabilizing/Petrov-Galerkin) stabilization technique (Tezduyar, Mittal, Ray, and Shih (1992)) is employed to stabilize the computations against spurious numerical oscillations. The formulation for the linear stability analysis with the stabilized finite element method, being used here, was proposed in one of our earlier articles (Mittal and Kumar (2003)). The linear stability analysis involves the solution to an eigenvalue problem. A sub-space iteration procedure (Morzynski, Afanasiev, and Thiele (1999)) in conjunction with shift-invert transformation is utilized.

2 The Governing Equations

2.1 The incompressible flow equations

We begin by reviewing the equations governing the flow of an incompressible fluid:

$$\rho(\frac{\partial \mathbf{u}}{\partial t} + \mathbf{u} \cdot \boldsymbol{\nabla}\mathbf{u} - \mathbf{f}) - \boldsymbol{\nabla} \cdot \boldsymbol{\sigma} = 0, \tag{1}$$

$$\boldsymbol{\nabla} \cdot \mathbf{u} = 0. \tag{2}$$

Here ρ, $\mathbf{u}$, $\mathbf{f}$ and $\boldsymbol{\sigma}$ are the density, velocity, body force and the stress tensor, respectively. The stress tensor is written as the sum of its isotropic and deviatoric parts: $\boldsymbol{\sigma} = -p\mathbf{I} + \mathbf{T}$, where, $\mathbf{T} = \mu((\boldsymbol{\nabla}\mathbf{u}) + (\boldsymbol{\nabla}\mathbf{u})^T)$. Here p and μ are the pressure and coefficient of dynamic viscosity, respectively. These equations are accompanied with appropriate boundary conditions on the velocity and stress and an initial condition on the velocity.

2.2 Linearized Disturbance Equations (LDE) and Linear Stability Analysis (LSA) of the flow

To derive the equations for disturbance field, the unsteady flow is expressed as a combination of the steady flow and the disturbance: $\mathbf{u} = \mathbf{U} + \mathbf{u}'$ and $p = P + p'$. Here, $(\mathbf{U}, P)$ represent the steady-state solution obtained by solving Eqs. (1) and (2) without the unsteady terms. $\mathbf{u}'$ and p' are the perturbation fields of the velocity and pressure, respectively. Substituting for this flow decomposition in Eqs. (1)-(2) and subtracting from them, the

equations for steady flow, one obtains the following equations for the disturbance fields:

$$\rho(\frac{\partial \mathbf{u}'}{\partial t} + \mathbf{u}' \cdot \boldsymbol{\nabla}\mathbf{U} + \mathbf{U} \cdot \boldsymbol{\nabla}\mathbf{u}' + \mathbf{u}' \cdot \boldsymbol{\nabla}\mathbf{u}') - \boldsymbol{\nabla} \cdot \boldsymbol{\sigma}' = 0, \tag{3}$$

$$\boldsymbol{\nabla} \cdot \mathbf{u}' = 0. \tag{4}$$

Here, $\boldsymbol{\sigma}'$ is the stress tensor due to the perturbed solution $(\mathbf{u}', p')$. We further assume that the disturbances are small and drop the non-linear term. This leads to the Linearized Disturbance Equations (LDE) of the form:

$$\rho(\frac{\partial \mathbf{u}'}{\partial t} + \mathbf{u}' \cdot \boldsymbol{\nabla}\mathbf{U} + \mathbf{U} \cdot \boldsymbol{\nabla}\mathbf{u}') - \boldsymbol{\nabla} \cdot \boldsymbol{\sigma}' = 0, \tag{5}$$

$$\boldsymbol{\nabla} \cdot \mathbf{u}' = 0. \tag{6}$$

For conducting the linear stability analysis (LSA) we assume the disturbance field to have the form: $\mathbf{u}'(\mathbf{x},t) = \hat{\mathbf{u}}(\mathbf{x})e^{\lambda t}$, $p'(\mathbf{x},t) = \hat{p}(\mathbf{x})e^{\lambda t}$. This allows us to conduct a global, linear stability analysis of a general, non-parallel but steady flow. Substituting this form of the disturbance in Eqs. (5)-(6) we get:

$$\rho(\lambda\hat{\mathbf{u}} + \hat{\mathbf{u}} \cdot \boldsymbol{\nabla}\mathbf{U} + \mathbf{U} \cdot \boldsymbol{\nabla}\hat{\mathbf{u}}) - \boldsymbol{\nabla} \cdot \hat{\boldsymbol{\sigma}} = 0 \tag{7}$$

$$\boldsymbol{\nabla} \cdot \hat{\mathbf{u}} = 0. \tag{8}$$

Here, λ is the eigenvalue of the fluid system and governs its stability. In general, $\lambda = \lambda_r + i\lambda_i$ where, λ_r and λ_i are the real and imaginary parts, respectively. The boundary conditions for $(\hat{\mathbf{u}}, \hat{p})$ are the homogeneous versions of the ones for $(\mathbf{U}, P)$.

2.3 Equations for the time-averaged flow and their stability

For an unsteady flow, one can also express the velocity and pressure fields as a combination of the time-averaged solution and the disturbance field (Mittal (2008)): $\mathbf{u} = \overline{\mathbf{u}} + \mathbf{u}''$, $p = \overline{p} + p''$. Here, $(\overline{\mathbf{u}}, \overline{p})$ represent the time-averaged flow while $\mathbf{u}''$ and p'' are the perturbation fields, with respect to $(\overline{\mathbf{u}}, \overline{p})$, of the velocity and pressure, respectively. On substituting this flow decomposition in Eqs. (1)-(2), and then time averaging them,

one obtains the Reynolds Averaged Navier Stokes equations (RANS):

$$\rho(\overline{\mathbf{u}} \cdot \nabla \overline{\mathbf{u}}) - \nabla \cdot \overline{\boldsymbol{\sigma}} = -\rho \nabla \cdot \overline{\mathbf{u}''\mathbf{u}''}, \tag{9}$$

$$\nabla \cdot \overline{\mathbf{u}} = 0. \tag{10}$$

Here, $\overline{\boldsymbol{\sigma}}$ is the stress tensor for the time-averaged flow, $(\overline{\mathbf{u}}, \overline{p})$. $-\rho\overline{\mathbf{u}''\mathbf{u}''}$ is the Reynolds stress tensor arising from the non-linearities in the advection term. Often, for computing time-averaged turbulent flows, the Reynolds stress are represented in terms of the time-averaged flow variables via a turbulence model. We subtract Eqs. (9)-(10) from Eq. (1)-(2) to obtain the time evolution equations for the disturbance field $(\mathbf{u}'', p'')$:

$$\rho(\frac{\partial \mathbf{u}''}{\partial t} + \mathbf{u}'' \cdot \nabla \overline{\mathbf{u}} + \overline{\mathbf{u}} \cdot \nabla \mathbf{u}'') - \nabla \cdot \boldsymbol{\sigma}'' = \rho \nabla \cdot \overline{\mathbf{u}''\mathbf{u}''}, \tag{11}$$

$$\nabla \cdot \mathbf{u}'' = 0. \tag{12}$$

Here, $\boldsymbol{\sigma}''$ is the stress tensor for the perturbations, $(\mathbf{u}'', p'')$, in the flow. In Eq. (11) the right hand side depends on the Reynolds stress. This is a known quantity for the time evolution of disturbance using this equation. In addition, for small disturbance the nonlinear term, $\mathbf{u}'' \cdot \nabla \mathbf{u}''$, is dropped from the left hand side of the equation. For future use in the paper we refer to these equations as the Linearized Disturbance Equations about Average (LDEA). The solution to Eqs. (11)-(12) is the combination of the homogeneous and the particular solutions. We observe that the homogeneous version of Eqs. (11)-(12) are identical to linearized version of Eqs. (3)-(4). Therefore, the stability of the time-averaged solution can be analyzed in a manner very similar to that for the steady-state flow. In certain situations, such as high *Re* flows, it is very difficult and sometimes even impossible to obtain a steady-state solution. However, it is significantly easier to generate a time-averaged solution using RANS (Eqs. (9)-(10)). The present analysis shows that, in such situations, the linear stability analysis of the time-averaged flow can be carried out to assess its stability. In this paper we will restrict ourselves to laminar flows and utilize these observations to investigate the $Re = 100$ flow past a cylinder.

3 Proper Orthogonal Decomposition (POD)

In the present work the snapshots from the direct time integration of the flow equations are utilized to generate the Karhunen-Loéve modes. Let $\mathbf{u}^i$ represent the ith of the N snapshots of the flow $\mathbf{u}(\mathbf{x}, t)$ and $\mathbf{u}^{[i]}(\mathbf{x})$ be the ith of the N Karhunen-Loéve modes of the flow. Using the N snapshots of the flow we can approximate it as:

$$\mathbf{u}(\mathbf{x}, t) \sim \overline{\mathbf{u}}(\mathbf{x}) + \sum_{i=1}^{N} a_i(t)\mathbf{u}^{[i]}(\mathbf{x}) \tag{13}$$

Here, $\overline{\mathbf{u}}(\mathbf{x})$ is the mean flow and $a_i(t)$ the time dependent Fourier coefficients which can be expressed as:

$$a_i = (\mathbf{u} - \overline{\mathbf{u}}, \mathbf{u}^{[i]})_{\Omega}, \tag{14}$$

where, $(\mathbf{v}, \mathbf{w})_{\Omega} = \int_{\Omega} \mathbf{v} \cdot \mathbf{w} \, d\Omega$ is the inner product between two divergence free fields $\mathbf{v}$ and $\mathbf{w}$. A temporal correlation matrix, $\mathbf{K}$ is constructed from the snapshots of the flow. Its components are given as

$$K_{ij} = (\mathbf{u}^i - \overline{\mathbf{u}}, \mathbf{u}^j - \overline{\mathbf{u}})_{\Omega}. \tag{15}$$

After forming $\mathbf{K}$ we compute its eigenvalues, λ_i, and eigenvectors. The eigenvectors are utilized to compute the Karhunen-Loéve modes (Sirovich (1987); Noack, Afanasiev, Morzynski, Tadmor, and Thiele (2003); Hasan and Sanghi (2007)). Half the value of each eigenvalue $(\lambda_i/2)$ represents the kinetic energy of the ith Karhunen-Loéve mode.

4 Problem set up and boundary conditions

The cylinder resides in a computational domain whose outer boundary is a rectangle. All the boundaries are located at a distance of $50D$ from the center of the cylinder, where D is the diameter of the cylinder. The radius of the cylinder is 1 unit; time is non-dimensionalized using the free-stream speed and the radius of the cylinder. The finite element mesh, used in this work, consists of $19,696$ quadrilateral elements and $20,034$ nodes. The structure of the mesh is same as the one used in our earlier studies (for example, Mittal and Kumar (2003)). A picture of the mesh is
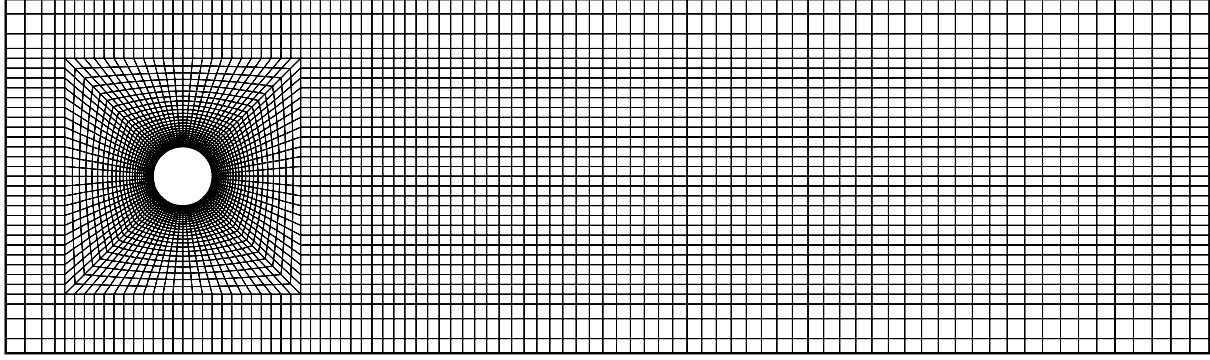
Figure 1: $Re = 100$ flow past a cylinder: a close-up view of the finite element mesh with $20,034$ nodes and $19,696$ quadrilateral elements.

shown in Figure 1. The following boundary conditions are applied. Free-stream value is assigned to the velocity at the upstream boundary. At the downstream boundary, a Neumann-type boundary condition for the velocity is specified that corresponds to zero stress vector. On the upper and lower boundaries a "slip-wall" boundary condition is employed, i.e., the component of velocity normal to and the component of stress vector along these boundaries are prescribed a zero value. For the linear stability analysis, as well as the disturbance equations, the boundary conditions are the homogeneous versions of the ones used for determining the steady state solutions.

5 The finite element formulation

5.1 The Incompressible Flow Equations

Consider a finite element discretization of the domain, Ω, into subdomains Ω^e, $e = 1, 2, ..., n_{el}$, where n_{el} is the number of elements. Based on this discretization let $\mathscr{S}_{\mathbf{u}}^h$ and $\mathscr{S}_p^h$ be the finite element trial function spaces for velocity and pressure, respectively and $\mathscr{V}_{\mathbf{u}}^h$ and $\mathscr{V}_p^h$ be the weighting function spaces. The stabilized finite element formulation of Eqs. (1)-(2) is written as follows: find $\mathbf{u}^h \in \mathscr{S}_{\mathbf{u}}^h$ and $p^h \in \mathscr{S}_p^h$ such that $\forall \mathbf{w}^h \in \mathscr{V}_{\mathbf{u}}^h$, $q^h \in \mathscr{V}_p^h$

$$
\int_\Omega \mathbf{w}^h \cdot \rho \left(\frac{\partial \mathbf{u}^h}{\partial t} + \mathbf{u}^h \cdot \boldsymbol{\nabla} \mathbf{u}^h - \mathbf{f} \right) d\Omega
$$

$$
+ \int_\Omega \boldsymbol{\varepsilon}(\mathbf{w}^h) : \boldsymbol{\sigma}(p^h, \mathbf{u}^h) d\Omega
$$

$$
+ \int_\Omega q^h \boldsymbol{\nabla} \cdot \mathbf{u}^h d\Omega
$$

$$
+ \sum_{e=1}^{n_{el}} \int_{\Omega^e} \frac{1}{\rho} \left(\tau_{\mathrm{SUPG}} \rho \mathbf{u}^h \cdot \boldsymbol{\nabla} \mathbf{w}^h + \tau_{\mathrm{PSPG}} \boldsymbol{\nabla} q^h \right) \cdot
$$

$$
\left[\rho \left(\frac{\partial \mathbf{u}^h}{\partial t} + \mathbf{u}^h \cdot \boldsymbol{\nabla} \mathbf{u}^h - \mathbf{f} \right) - \boldsymbol{\nabla} \cdot \boldsymbol{\sigma}(p^h, \mathbf{u}^h) \right] d\Omega^e
$$

$$
+ \sum_{e=1}^{n_{el}} \int_{\Omega^e} \tau_{\mathrm{LSIC}} \boldsymbol{\nabla} \cdot \mathbf{w}^h \rho \boldsymbol{\nabla} \cdot \mathbf{u}^h d\Omega^e
$$

$$
= \int_{\Gamma_h} \mathbf{w}^h \cdot \mathbf{h}^h d\Gamma. \quad (16)
$$

Here, Γ_g and Γ_h are complementary subsets of the boundary Γ on which Dirichlet and Neumann-type boundary conditions are assigned as follows:

$$
\mathbf{u} = \mathbf{g} \ on \ \Gamma_g, \quad \mathsf{n} \cdot \boldsymbol{\sigma} = \mathbf{h} \ on \ \Gamma_h, \quad (17)
$$

where, n is the unit normal vector to Γ_h. In the variational formulation given by Eqn. (16), the first three terms and the right-hand side constitute the Galerkin formulation of the problem. It is well known that the Galerkin formulation is unstable with respect to the advection operator as the cell Reynolds number(based on the local flow velocity and mesh size) becomes larger. Also, not all combinations of the velocity and pressure interpolations are admissible in the Galerkin

formulation. Elements that do not satisfy the Babuska-Brezzi condition lead to oscillatory solutions and, sometimes, no solution at all. For example, the equal-order interpolations for velocity and pressure lead to oscillatory solutions if they are used with a Galerkin formulation. To give stability to the basic Galerkin formulation, a series of element-level integrals are added. The first series of element-level integrals are the SUPG and PSPG stabilization terms added to the variational formulations (Tezduyar, Mittal, Ray, and Shih (1992)). The SUPG formulation for convection dominated flows was introduced by Hughes and Brooks (1979) and Brooks and Hughes (1982). The Petrov-Galerkin term for Stokes flows, to admit the use of equal-order interpolations for velocity and pressure without producing oscillations in the pressure field, was proposed by Hughes, Franca, and Balestra (1986). Tezduyar, Mittal, Ray, and Shih (1992) proposed a formulation using the SUPG and PSPG stabilizations for finite Reynolds number flows. The second series of element level integrals are stabilization terms based on the least squares of the divergence-free condition on the velocity field. The definition for τ_{PSPG} and τ_{SUPG} is given by the following relations based on its values for the advection and diffusion limits.

$$\tau_{\text{SUPG}} = \tau_{\text{PSPG}} = \left(\frac{1}{\tau_{\text{ADV}}^2} + \frac{1}{\tau_{\text{DIF}}^2} \right)^{-\frac{1}{2}}, \tag{18}$$

where,

$$\tau_{\text{ADV}} = \frac{h^e}{2\|\mathbf{u}^h\|}, \tau_{\text{DIF}} = \frac{(h^e)^2}{12\nu}. \tag{19}$$

Here, h^e is the element length and various definitions have been used by researchers in the past. Mittal (2000) conducted a systematic numerical study to investigate the effect of high aspect ratio elements on the performance of the finite element formulation for three commonly used definitions of h^e. In this work we use the definition based on the minimum edge length of an element. The coefficient τ_{LSIC} is defined as

$$\tau_{\text{LSIC}} = \left(\frac{1}{\delta_{\text{ADV}}^2} + \frac{1}{\delta_{\text{DIF}}^2} \right)^{-\frac{1}{2}}, \tag{20}$$

where

$$\delta_{\text{ADV}} = \frac{h^e\|\mathbf{u}^h\|}{2}, \delta_{\text{DIF}} = \frac{(h^e)^2(\|\mathbf{u}^h\|)^2}{12\nu}. \tag{21}$$

The nonlinear equation system resulting from the finite element discretization of the flow equations are solved using the Generalized Minimal RESidual (GMRES) technique (Saad and Schultz (1986)) in conjunction with diagonal preconditioners. The implicit method used in the present work allows us to seek steady-state solutions by simply dropping the unsteady terms in the governing equations. Several alternate formulations for solving the unsteady flow equations exist. Some examples can be found in the work by Nicolas and Bermudez (2007) and Mai-Duy, Mai-Cao, and Tran-Cong (2007).

5.2 The Equations for Linear Stability Analysis

Let $\hat{\mathscr{S}}_{\mathbf{u}}^h$ and $\hat{\mathscr{S}}_p^h$ be the finite element trial function spaces and $\hat{\mathscr{V}}_{\mathbf{u}}^h$ and $\hat{\mathscr{V}}_p^h$ the weighting function spaces for the perturbations in the velocity and pressure fields, respectively. The finite element formulation for the perturbation equations, (7) and (8), is given as: find $\hat{\mathbf{u}}^h \in \hat{\mathscr{S}}_{\mathbf{u}}^h$ and $\hat{p}^h \in \hat{\mathscr{S}}_p^h$ such that $\forall \hat{\mathbf{w}}^h \in \hat{\mathscr{V}}_{\mathbf{u}}^h$ and $\hat{q}^h \in \hat{\mathscr{V}}_p^h$

$$\int_{\Omega} \hat{\mathbf{w}}^h \cdot \rho \left(\lambda \hat{\mathbf{u}}^h + \mathbf{U}^h \cdot \boldsymbol{\nabla} \hat{\mathbf{u}}^h + \hat{\mathbf{u}}^h \cdot \boldsymbol{\nabla} \mathbf{U}^h \right) d\Omega$$
$$+ \int_{\Omega} \boldsymbol{\varepsilon}(\hat{\mathbf{w}}^h) : \boldsymbol{\sigma}(\hat{p}^h, \hat{\mathbf{u}}^h) d\Omega$$
$$+ \int_{\Omega} \hat{q}^h \boldsymbol{\nabla} \cdot \hat{\mathbf{u}}^h d\Omega$$
$$+ \sum_{e=1}^{n_{el}} \int_{\Omega^e} \frac{1}{\rho} \left(\tau_{\text{SUPG}} \rho \mathbf{U}^h \cdot \boldsymbol{\nabla} \hat{\mathbf{w}}^h + \tau_{\text{PSPG}} \boldsymbol{\nabla} \hat{q}^h \right) \cdot$$
$$\left[\rho \left(\lambda \hat{\mathbf{u}}^h + \mathbf{U}^h \cdot \boldsymbol{\nabla} \hat{\mathbf{u}}^h + \hat{\mathbf{u}}^h \cdot \boldsymbol{\nabla} \mathbf{U}^h \right) \right.$$
$$\left. - \boldsymbol{\nabla} \cdot \boldsymbol{\sigma}(\hat{p}^h, \hat{\mathbf{u}}^h) \right] d\Omega^e$$
$$+ \sum_{e=1}^{n_{el}} \int_{\Omega^e} \tau_{\text{LSIC}} \boldsymbol{\nabla} \cdot \hat{\mathbf{w}}^h \rho \boldsymbol{\nabla} \cdot \hat{\mathbf{u}}^h d\Omega^e = 0. \tag{22}$$

The stabilization coefficients for the linear stability analysis are given by the same definition as defined in Equations (18)-(21) except that they are

based on the steady-state velocity field, $\mathbf{U}^h$. Equation (22) leads to a generalized eigenvalue problem of the form $\mathbf{A}X - \lambda \mathbf{B}X = 0$, where $\mathbf{A}$ and $\mathbf{B}$ are nonsymmetric matrices. In this study we use the shift-invert transformation in conjunction with the subspace iteration method (Stewart (1975)) to track the eigenvalue with the largest real part.

6   Results: $Re = 100$ flow past a cylinder

6.1   2D Direct Numerical Simulation (DNS)

The steady-state solution to Eqs. (1)-(2) is computed by dropping the unsteady terms. The vorticity field for the steady flow past a cylinder for $Re = 100$ is shown in the top row of Figure 2. The unsteady flow past a cylinder is obtained via time integration of Eqs.(1-2) with a time step size of 0.10 (non-dimensional units). The computations begin with a steady state flow. Two strategies were tried to achieve a fully developed unsteady flow. In the first method, the vortex shedding is excited by perturbing the flow via rotating the cylinder. First, the cylinder is rotated clockwise for 10 time steps with a rotation rate that corresponds to a tip speed that is 10% of the free-stream speed. This is followed by a counterclockwise rotation for 5 time-steps with twice the rotation rate. The cylinder, then, remains stationary and the unsteady flow is allowed to develop for the uniform inflow. In the second method the computations begin by adding a small random disturbance (of the order of half the machine precision $\sim 10^{-6}$) to the steady solution. Both methods lead to the same developed unsteady flow. The results shown in this paper are the ones obtained with the latter strategy. The vorticity field for the fully developed unsteady flow is shown in the middle row of Figure 2. The lowest panel in this figure shows the disturbance field obtained by subtracting the steady flow from the instantaneous fully developed unsteady flow. Throughout this paper, the magnitude of a flow quantity is displayed in gray-scale: darker the shade, larger is the magnitude. White contour lines indicate a positive value while the black ones represent negative value.

The St, corresponding to the vortex shedding frequency, is 0.163. As a result of the unsteady flow, the cylinder experiences time-varying lift and drag forces. The amplitude of the lift coefficient is 0.309. The time histories of the drag and lift coefficients are shown in Figure 3. Computations with a finer mesh, with 40,000 quadrilateral elements and 40,480 nodes, result in $St = 0.164$, and an amplitude of lift coefficient of 0.319. These values are in excellent agreement with already published data. For example, Kravchenko, Moin, and Shariff (1999) used a B-Spline method in conjunction with zonal grids to compute flow past a cylinder up to $Re = 300$. For the $Re = 100$ flow, they report the Strouhal number to be 0.164 and the amplitude of the lift coefficient to be 0.314. Persillon and Braza (1998) have reported a parallel, 2D type vortex shedding for their simulations with slip end-walls at $Re = 100$ and $L/D = 2.25$. From their computations the Strouhal number is 0.164. Williamson (1989) measured $St = 0.1648$ for parallel shedding.

The fully developed unsteady solution obtained from the direct numerical simulation is time-averaged for, approximately, 75 vortex shedding cycles. The Reynolds stresses ($\overline{u''u''}$, $\overline{u''v''}$ and $\overline{v''v''}$) are shown in Figure 4. Compared to the far wake, the Reynolds stresses are more significant in the near wake of the cylinder. As a result of these stresses the time-averaged drag coefficient is significantly larger than the one for the steady-state flow. This can be observed from the time history of the drag coefficient shown in Figure 3. The distribution of the Reynolds stresses is in good agreement with the computational results of Mittal and Balachander (1995). The vorticity field for the time-averaged flow is shown in Figure 5. Compared to the steady flow, the time-averaged flow is associated with a much smaller recirculating flow bubble. Although the region of high vorticity is restricted to the very near wake, the lateral width of the wake of the time-averaged flow is slightly larger than the one for steady flow. Also shown in this figure is the disturbance field with respect to the time-averaged flow. The instantaneous flow for which the disturbance field is shown corresponds to the unsteady flow shown in Figure 2.
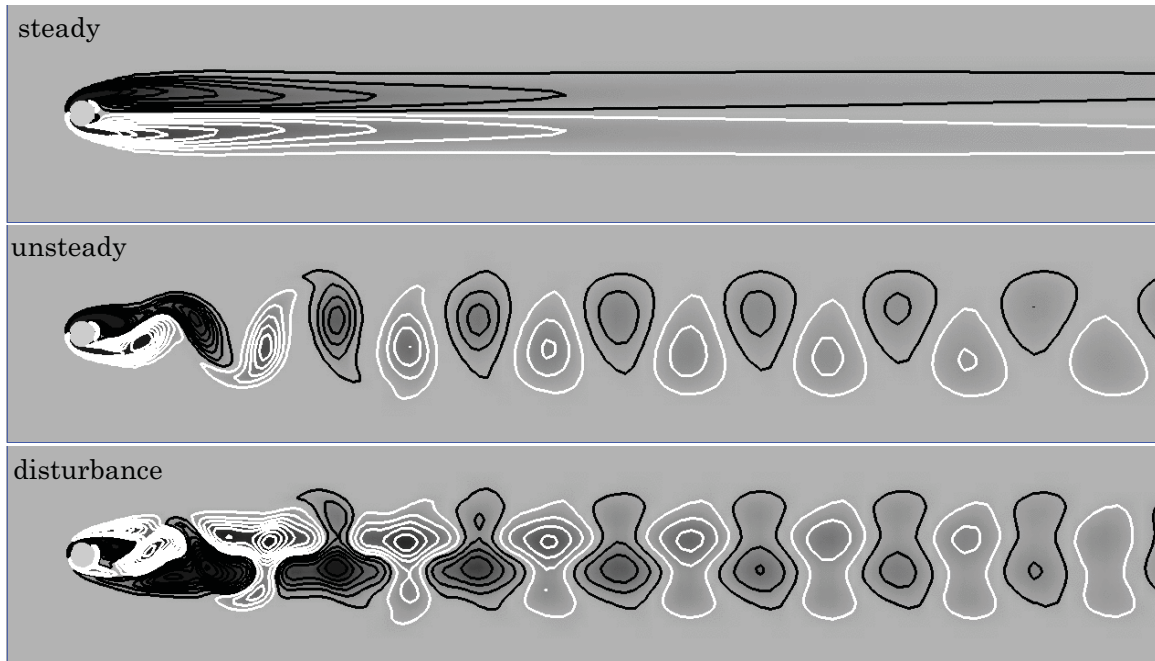
Figure 2: $Re = 100$ flow past a cylinder: vorticity field of the fully developed steady (top), unsteady flow (middle) and the disturbance (below).
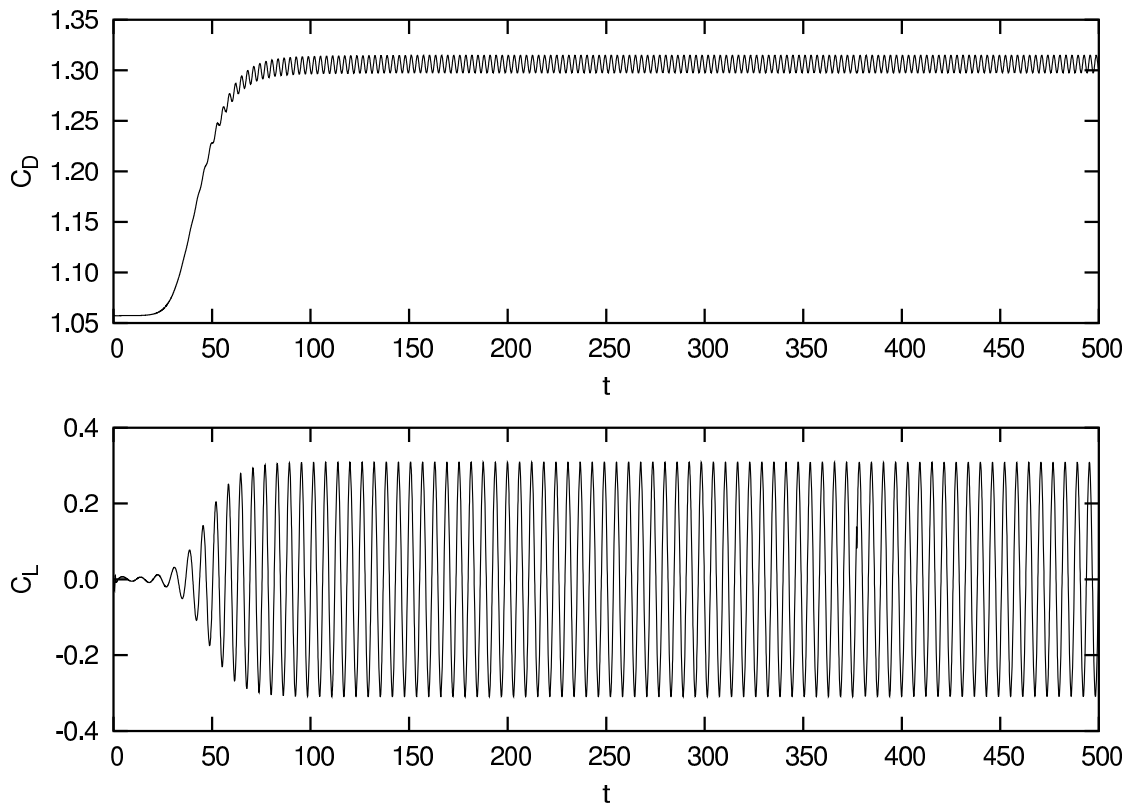

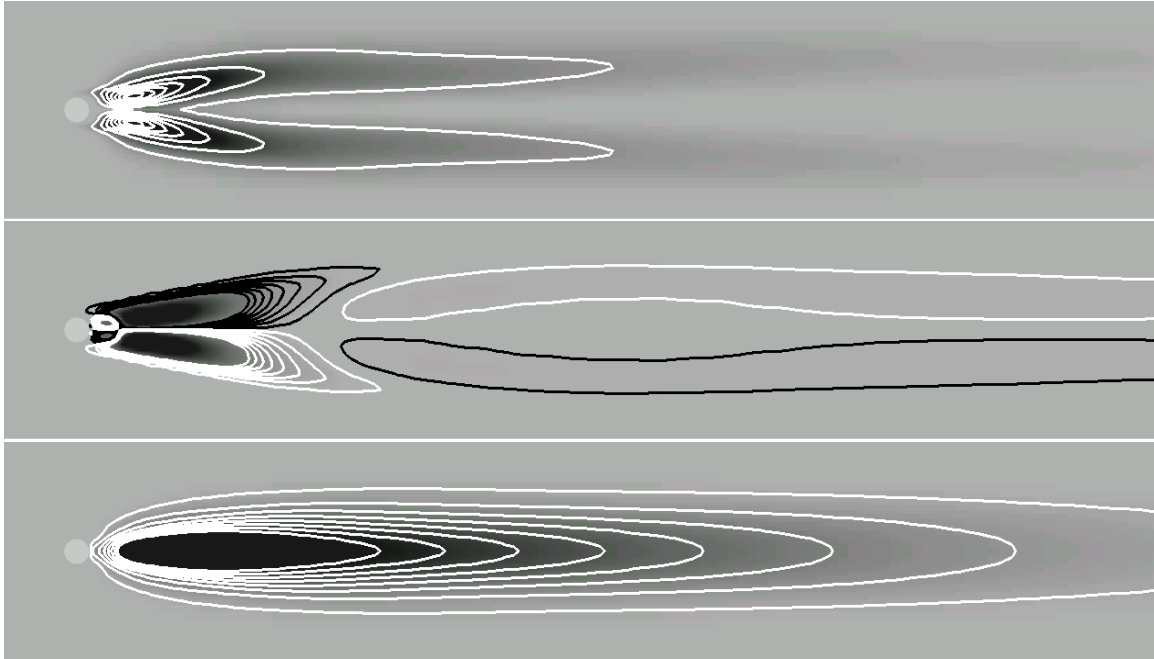Figure 3: $Re = 100$ flow past a cylinder: time histories of the drag and lift coefficients.

Figure 4: $Re = 100$ flow past a cylinder: (from top to bottom) Reynolds stresses $\overline{u''u''}$, $\overline{u''v''}$ and $\overline{v''v''}$ for the unsteady flow.
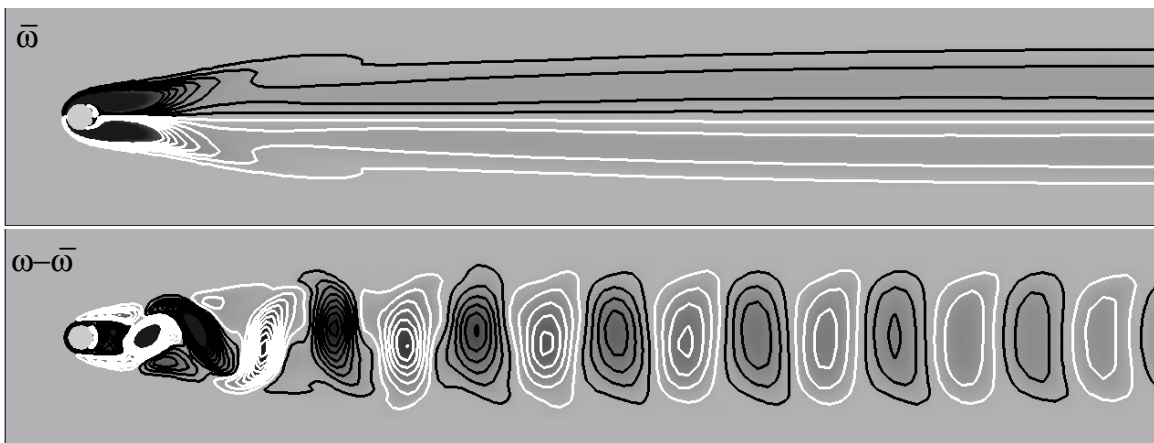

Figure 5: $Re = 100$ flow past a cylinder: vorticity fields of the time-averaged unsteady flow (top) and the disturbance field with respect to the time-averaged flow. The instantaneous flow for which the disturbance field is shown corresponds to the unsteady flow shown in Figure 2.

6.2 Linear stability analysis of the steady flow

A linear stability analysis for the $Re = 100$ steady flow past a cylinder is carried out. As expected, the LSA predicts the flow to be unstable. Figure 6 shows the vorticity field for the real and imaginary parts of the most unstable eigenmode. While the steady-state vorticity field is anti-symmetric with respect to the flow axis, the perturbation field is symmetric. A linear combination of the two results in a non-symmetric field that resembles the von Karman vortex shedding as shown in Fig-
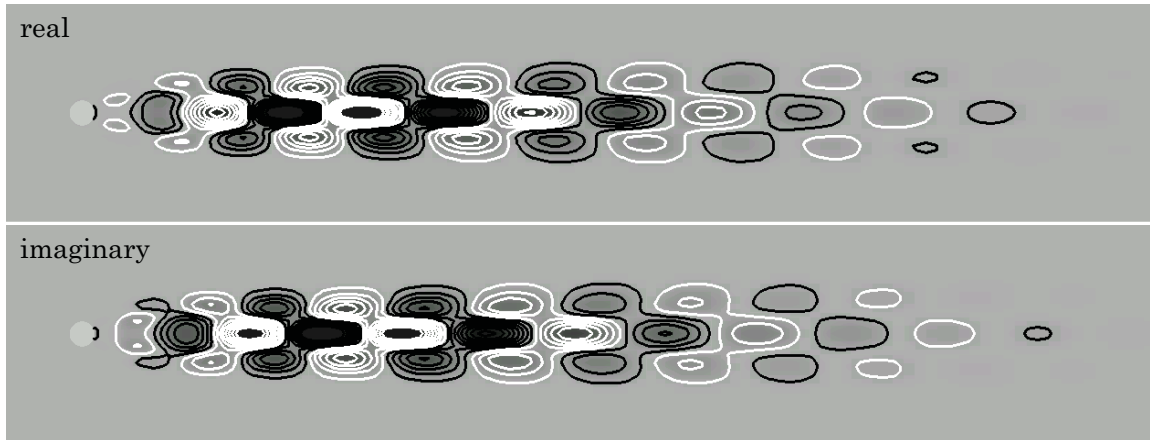
Figure 6: Linear stability analysis of the steady $Re = 100$ flow past a cylinder: vorticity fields of the real and imaginary parts of the most unstable eigen-mode.
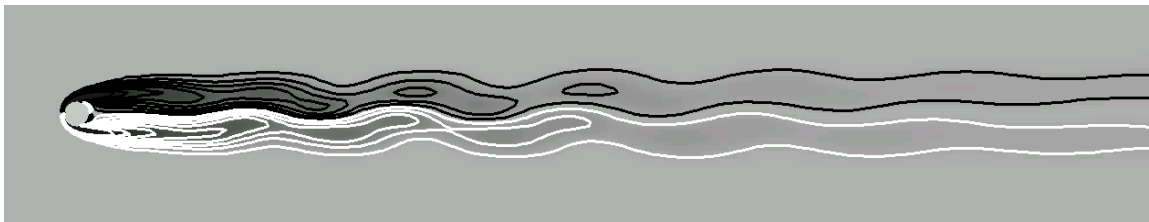

Figure 7: $Re = 100$ flow past a cylinder: vorticity field of obtained from the linear combination of the steady-state flow and the eigenmodes corresponding to the most unstable conjugate pair of eigenvalues.

ure 7. The vorticity field shown in the figure corresponds to the flow at $t = 9$ obtained from $\mathbf{U}(\mathbf{x}) + \hat{\mathbf{u}}(\mathbf{x})e^{\lambda t} + \overline{\hat{\mathbf{u}}}(\mathbf{x})e^{\overline{\lambda} t}$. Here, $\hat{\mathbf{u}}(\mathbf{x})$ and $\overline{\hat{\mathbf{u}}}(\mathbf{x})$ are the eigen-functions corresponding to the conjugate pair of the most unstable eigen-values (λ and $\overline{\lambda}$). The St corresponding to the most unstable mode is 0.115 while its growth rate is $\lambda_r = 5.8 \times 10^{-2}$. This value of St is much lower than the actual shedding frequency (~ 0.164) observed from the direct numerical simulation. This is also observed from the difference between the longitudinal spacing of the vortices in the two cases. This reflects the inadequacy of the LSA of the steady-state flow in predicting the correct St. We have observed from our 2D direct numerical simulations that in the initial stages of the simulation, when the disturbances are weak, the shedding frequency is very close to 0.115. However, as the disturbances grow, the non-linear terms become

larger and modify the disturbance field including the shedding frequency. The finite element mesh that is being used in the computations here is sufficiently refine to capture all the details of the flow. We have experimented with more refined meshes; no significant change in the results was observed.

6.3 Time integration of Linear Disturbance Equations (LDE)

To study the effect of non-linear terms in the governing equations, and investigate the correctness of the results predicted from the the Linear Stability Analysis, direct time integration of the Linear Disturbance Equations (LDE, Eqn.(5)-6)) is carried out. The computations are initiated with the same random disturbance field as described in the previous section. The random disturbance excites several modes. However, most of them decay with time except the mode that is responsible for vor-
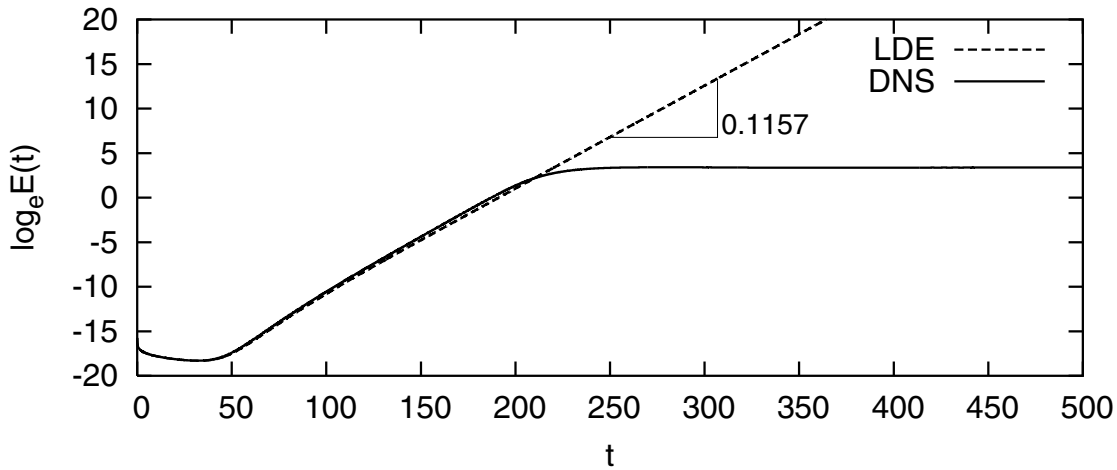
Figure 8: $Re = 100$ unsteady flow past a cylinder: time evolution of the kinetic energy of the disturbance obtained with Direct Numerical Simulation (DNS) and Linearized Disturbance Equations (LDE).

tex shedding. In the absence of the non-linear terms the flow does not reach a limit cycle and the disturbance field continues to grow exponentially with the growth rate predicted by the Linear Stability Analysis (LSA). As expected, after a certain number of time steps, the numbers become too large causing an 'overflow' and the program terminates. The disturbance field generated from the time integration of LDE are identical to to the modes predicted by LSA.

We define the kinetic energy of the disturbance in the computational domain as: $E(t) = 1/2 \int_{\Omega} \mathbf{u}' \cdot \mathbf{u}' d\Omega$. The time evolution of the energy of the disturbance, $E(t)$, is shown in Figure 8 with and without the non-linear terms. It can be observed that till $t \sim 200$, since the disturbance field is relatively small the effect of non-linear terms is negligible. Till this time the growth rate of the energy is ~ 0.1157. As expected, this is roughly twice the value of the growth rate of the disturbance $(\mathbf{u}', p')$ predicted by LSA. While the energy of the disturbance computed with the LDE continues to grow with this rate, the non-linear terms lead to a saturation of the energy extracted from the base flow thereby putting the fluid system through a limit cycle.

6.4 Linear stability analysis of the time-averaged flow

The vorticity field for the time-averaged flow for, approximately, 75 vortex shedding cycles is shown in Figure 5. In line with the homogeneous version of Eqs. (11)-(12), a linear stability analysis for this time-averaged flow is carried out. This flow is also found to be unstable, although it is associated with a very small growth rate ($\lambda_r = 3.2 \times 10^{-4}$). Interestingly, only one unstable mode (complex conjugate pair) is found and the St corresponding to the imaginary part of the eigenvalue is 0.16. Unlike the results from the LSA of the steady state flow, this value of St is in very good agreement with the actual vortex shedding frequency observed from the experiments and direct numerical simulations. The vorticity field corresponding to the real and imaginary parts of the most unstable eigenmode is shown in Figure 9. Shown in Figure 10 is the linear combination of the time-averaged flow and the eigenmodes corresponding to the most unstable pair of conjugate eigenvalues. Compared to the flow in Figure 7, from the steady-state analysis, this looks much closer to the solution from direct numerical simulation (Figure 2). The longitudinal spacing between the vortices, that is related to St, is quite
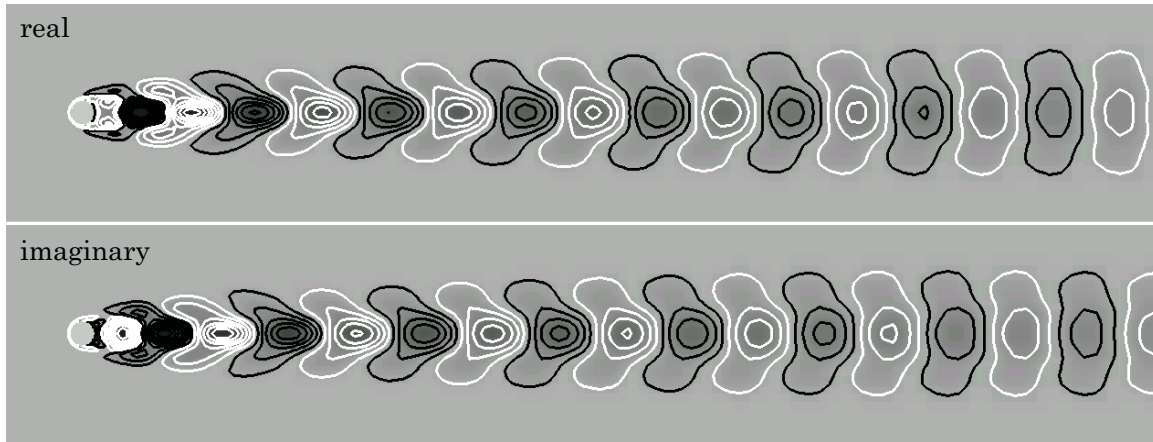
Figure 9: Linear stability analysis of the time-averaged $Re = 100$ flow past a cylinder: vorticity field of the real and imaginary parts of the most unstable eigen-mode.
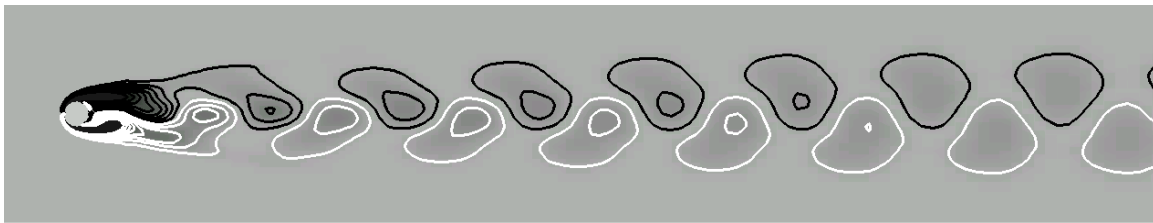

Figure 10: $Re = 100$ flow past a cylinder: vorticity field of obtained from the linear combination of the time-averaged flow and the eigenmodes corresponding to the most unstable conjugate pair of eigenvalues.

comparable in Figures 2 and 10.

6.5 Direct time integration of Linearized Disturbance Equations about Average (LDEA)

To further explore the relevance of the results from the linear stability analysis of time averaged flow, a direct time integration of the homogeneous form of LDEA (Eqns (11)-(12) without the Reynolds stress terms) is carried out. The base flow is the time averaged flow shown in Figure 5. Figure 11 shows the time evolution of the energy of the disturbance and lift coefficient due to the disturbance field. The energy of the disturbance field is defined as $E(t) = 1/2 \int_{\Omega} \mathbf{u}'' \cdot \mathbf{u}'' d\Omega$. Also shown in the figure is the instantaneous vorticity field of the disturbance. As expected, the disturbance field is very similar to the mode from the

LSA of the homogeneous version of the RANS. The growth rate of the energy, marked as the slope of the $log_e(E(t))$ *vs.* t in Figure 11, is nearly twice the value of the growth rate of $\mathbf{u}''$.

6.6 Proper Orthogonal Decomposition (POD)

In this work the Karhunen-Loéve modes are computed using 125 snapshots of the fully developed periodic unsteady flow which are uniformly sampled during two periods of the time variation of lift coefficient. It was shown by Deane, Kevrekidis, Karniadakis, and Orszag (1991) that 20 snapshots are enough to compute the first 8 Karhunen-Loéve modes of the flow. Figure 12 shows the first eight Karhunen-Loéve modes. It can be observed that the modes appear to form pairs. Each of the two modes of the pair seem quite similar albeit with a phase difference. This
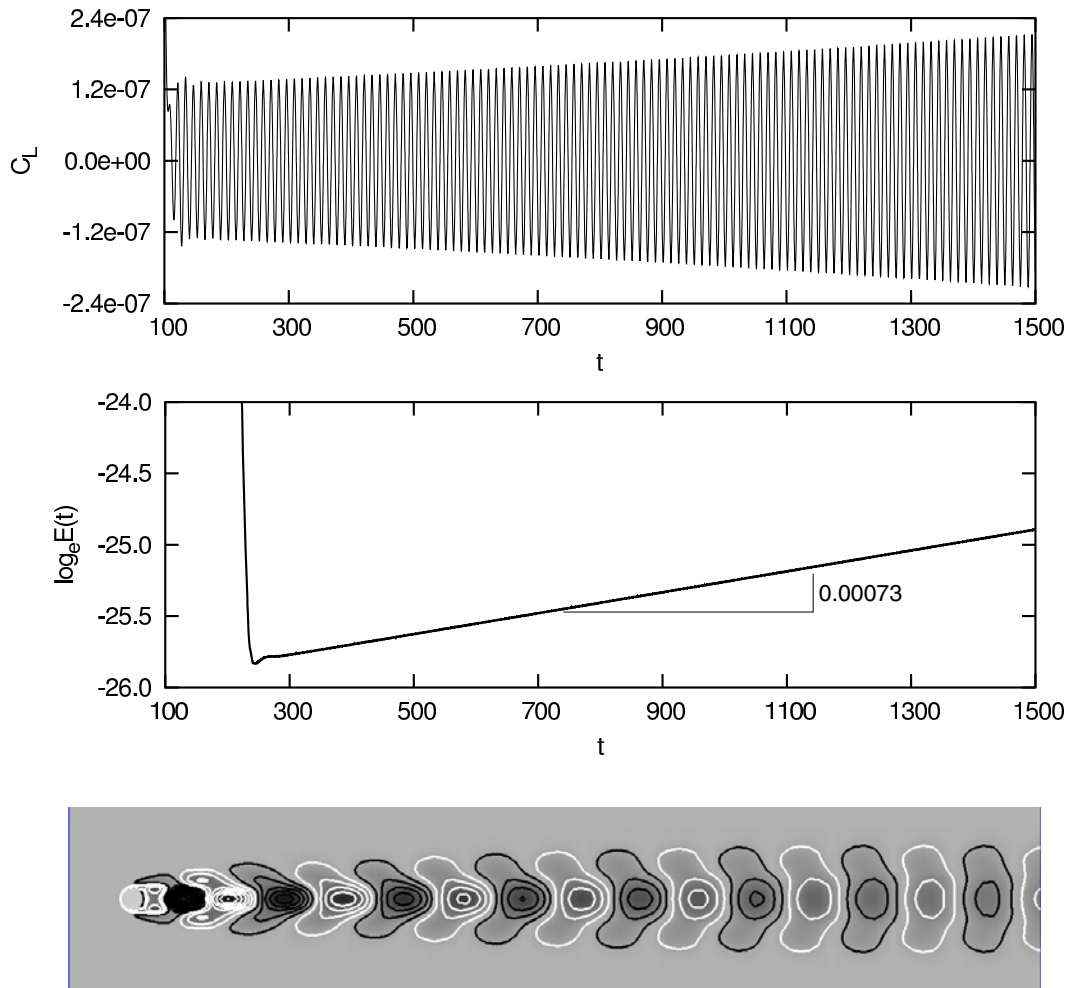
Figure 11: $Re = 100$ flow past a cylinder computed using the homogeneous form of the Linearized Disturbance Equations about Average (LDEA): time evolution of the energy of the disturbance and lift coefficient. Also shown is the instantaneous vorticity field of the disturbance.

is quite similar to the difference between the real and imaginary part of the complex eigenmodes obtained from the LSA. In addition, each alternate pair of modes is symmetric about the $x-axis$. These results are in very good agreement with those reported by Noack, Afanasiev, Morzynski, Tadmor, and Thiele (2003). Figure 13 shows the kinetic energy content in each of the first 15 modes of the flow. The energy in the ith mode is equal to $\lambda_i/2$, where, λ_i is the Karhunen-Loéve eigenvalue. Most of the energy is contained in the first pair of modes. On comparing the modes

from POD in Figure 12 and LSA of time-averaged flow in Figure 9 it can be seen that the two techniques result in different modes. Also shown in Figure 13 is the distribution of eigenvalues for the POD conducted for the snapshots of flow obtained from solving the Linearized Disturbance Equations (LDE, Eqns.(3)-(4)). As expected, the higher modes are much weaker for the linearized system. Also the strongest mode from POD is almost identical to the one predicted by LSA of steady state flow.

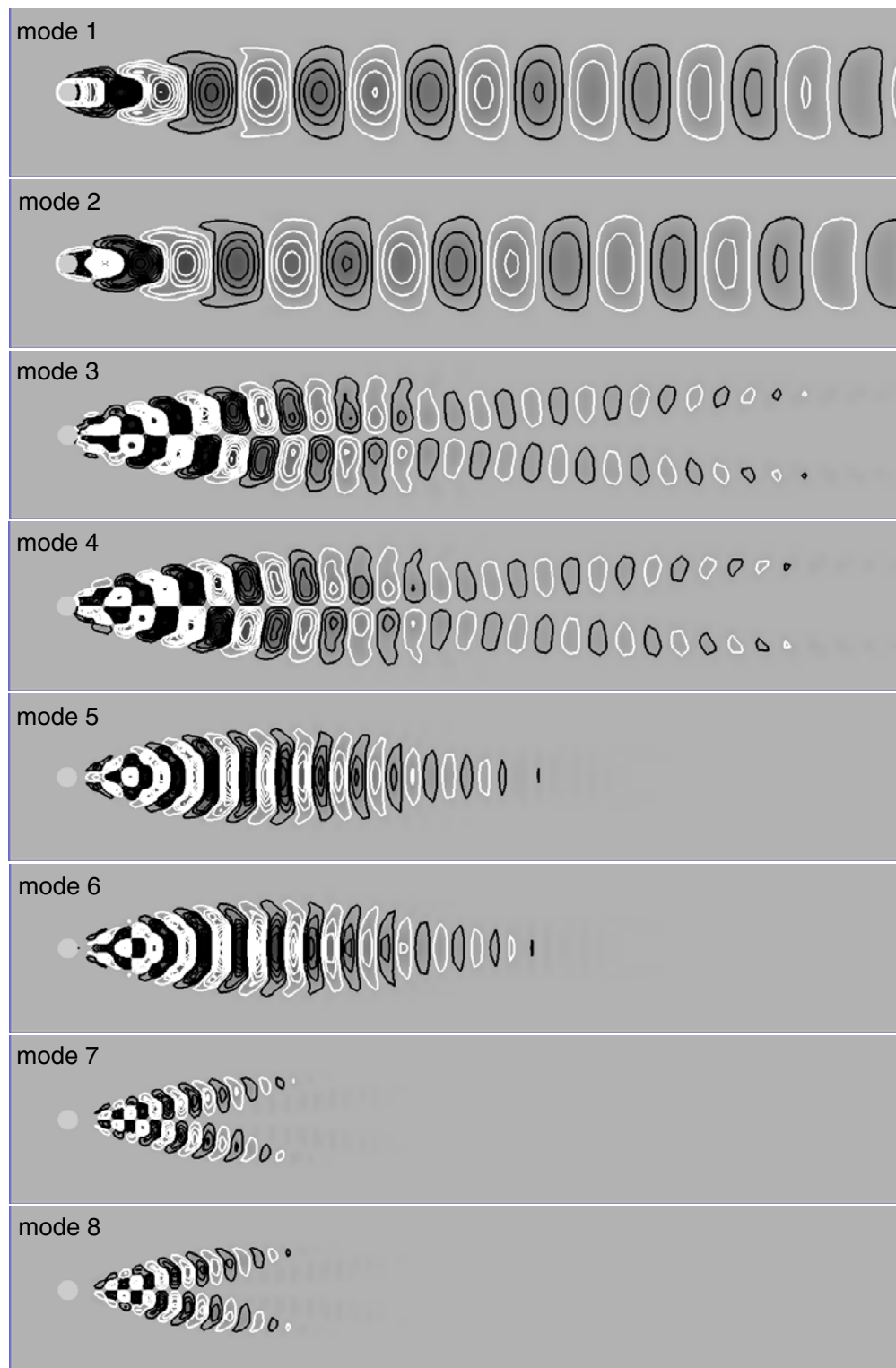One obvious advantage of LSA over POD is the

Figure 12: Proper Orthogonal Decomposition of the $Re = 100$ unsteady flow past a cylinder: the vorticity field for the first eight Karhunen-Loéve modes.
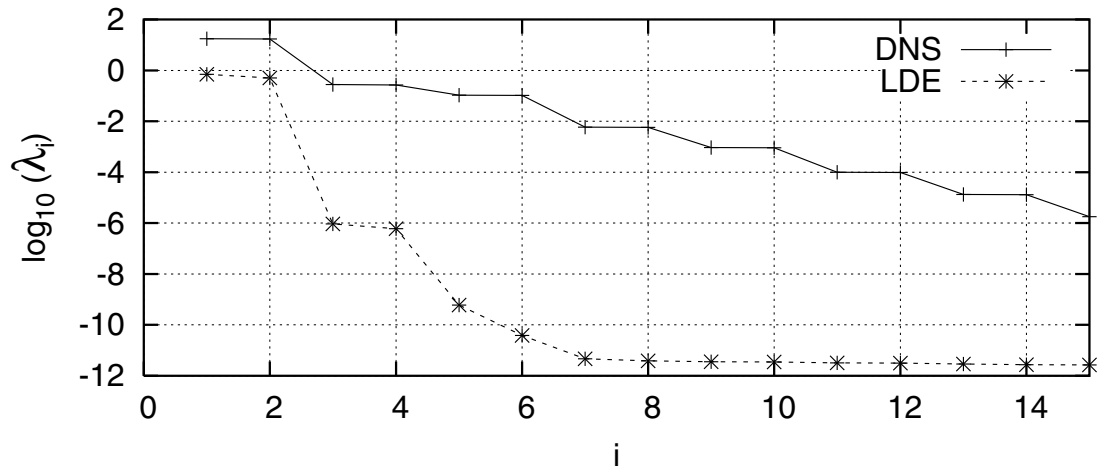
Figure 13: Proper Orthogonal Decomposition of the $Re = 100$ unsteady flow past a cylinder: eigenvalues corresponding to the first fifteen Karhunen-Loéve modes. Results are shown for flow snapshots obtained by solving the non-linear equations (DNS) as well as the Linearized Disturbance Equations (LDE).

information on Strouhal number that it provides. In this particular flow problem, the analysis utilizes the time-averaged unsteady solution which has been explicitly computed, and therefore, already known to be unstable. Nevertheless, the exercise demonstrates that the LSA can still provide useful information such as the dominant eigenvalues and eigenmodes. It also opens up the possibility of evaluating the stability of time-averaged flows computed via solutions to the RANS equations.

7   Concluding Remarks

Linear stability analysis of the $Re = 100$ flow past a circular cylinder has been carried out. LSA for the steady-state flow results in a significantly lower St as compared to the value from experiments and direct numerical simulations. LSA of the time-averaged flow results in the correct value of St. In many engineering situations, RANS equations in conjunction with a turbulence model are employed to calculate a time-averaged flow. In such situations, LSA can provide useful information regarding the stability of these flows. Proper Orthogonal (POD) or Karhunen-Loéve (K-L) decomposition of the unsteady flow

using the snapshot method is also carried out. The modes from this decomposition are compared to the unstable modes computed using the LSA. It is found that in the absence of non-linear terms in the disturbance equations the LSA and POD lead to very similar modes. However, in the presence of non-linear terms the mode shapes from the two methods are not same. One advantage of POD, over LSA is the information on the value of St that it provides.

References

Brooks, A.; Hughes, T. (1982):   Streamline upwind/Petrov-Galerkin formulations for convection dominated flows with particular emphasis on the incompressible Navier-Stokes equations. *Computer Methods in Applied Mechanics and En-*

gineering, vol. 32, pp. 199–259.

Deane, A.; Kevrekidis, I.; Karniadakis, G.; Orszag, S. (1991): Low-dimensional models for complex geometry flows: Application to grooved channels and circular cylinders. *Physics of Fluids A*, vol. 3, pp. 2337–2354.

Ding, Y.; Kawahara, M. (1999): Three dimensional linear stability analysis of incompressible viscous flows using the finite element method. *International Journal for Numerical Methods in Fluids*, vol. 31, pp. 451–479.

Hasan, N.; Sanghi, S. (2007): Proper orthogonal decomposition and low-dimensional modelling of thermally driven two-dimensonal flow in a horizontal rotating cylinder. *Journal of Fluid Mechanics*, vol. 573, pp. 265–295.

Hughes, T.; Brooks, A. (1979): A multidimensional upwind scheme with no crosswind diffusion. In Hughes, T.(Ed): *Finite Element Methods for Convection Dominated Flows*, AMD-Vol.34, pp. 19–35. ASME, New York.

Hughes, T.; Franca, L.; Balestra, M. (1986): A new finite element formulation for computational fluid dynamics: V. Circumventing the Babuška–Brezzi condition: A stable Petrov–Galerkin formulation of the Stokes problem accommodating equal-order interpolations. *Computer Methods in Applied Mechanics and Engineering*, vol. 59, pp. 85–99.

Jackson, C. (1987): A finite-element study of the onset of vortex shedding in flow past variously shaped bodies. *Journal of Fluid Mechanics*, vol. 182, pp. 23–45.

Kravchenko, A.; Moin, P.; Shariff, K. (1999): B-Spline method and zonal grids for simulations of complex turbulent flows. *Journal of Computational Physics*, vol. 151, pp. 757–789.

Kumar, B.; Mittal, S. (2006): Effect of blockage on critical parameters for flow past a circular cylinder. *International Journal for Numerical Methods in Fluids*, vol. 50, pp. 987–1001.

Mai-Duy, N.; Mai-Cao, L.; Tran-Cong, T. (2007): Computation of transient viscous flows using indirect radial basis function networks. *CMES: Computer Modeling in Engineering & Sciences*, vol. 18, no. 1, pp. 59–78.

Mittal, R.; Balachander, S. (1995): Effect of three-dimensionality on the lift and drag of nominally two-dimensional cylinders. *Physics of Fluids*, vol. 7, pp. 1841–1865.

Mittal, S. (2000): On the performance of high aspect-ratio elements for incompressible flows. *Computer Methods in Applied Mechanics and Engineering*, vol. 188, pp. 269–287.

Mittal, S. (2008): Global linear stability analysis of time-averaged flows. in press*International Journal for Numerical Methods in Fluids*, 2008.

Mittal, S.; Kumar, B. (2003): Flow past a rotating cylinder. *Journal of Fluid Mechanics*, vol. 476, pp. 303–334.

Morzynski, M.; Afanasiev, K.; Thiele, F. (1999): Solution of the eigenvalue problems resulting from global non-parallel flow stability analysis. *Computer Methods in Applied Mechanics and Engineering*, vol. 169, pp. 161–176.

Nicolas, A.; Bermudez, B. (2007): Viscous incompressible flows by the velocity-vorticity Navier-Stokes equations. *CMES: Computer Modeling in Engineering & Sciences*, vol. 20, no. 2, pp. 73–84.

Noack, B. R.; Afanasiev, K.; Morzynski, M.; Tadmor, G.; Thiele, F. (2003): A hierarchy of low-dimensional models for the transient and post-transient cylinder wake. *Journal of Fluid Mechanics*, vol. 497, pp. 335–363.

Persillon, H.; Braza, M. (1998): Physical analysis of the transition to turbulence in the wake of a circular cylinder by three-dimensional Navier-Stokes simulation. *Journal of Fluid Mechanics*, vol. 365, pp. 23–88.

Saad, Y.; Schultz, M. (1986): GMRES: A generalized minimal residual algorithm for solving nonsymmetric linear systems. *SIAM Journal*

of Scientific and Statistical Computing, vol. 7, pp. 856–869.

Sirovich, L. (1987):   Turbulence and the dynamics of coherent structures. i - coherent structures. *Quarterly of Applied Mathematics*, vol. 45, pp. 561–571.

Stewart, G. (1975):   Methods of simultaneous iteration for calculating eigenvectors of matrices. *Topics in Numerical Analysis II(ed. J.H.H. Miller),Academic*, pp. 169–185.

Tezduyar, T.; Mittal, S.; Ray, S.; Shih, R. (1992):   Incompressible flow computations with stabilized bilinear and linear equal-order-interpolation velocity-pressure elements. *Computer Methods in Applied Mechanics and Engineering*, vol. 95, pp. 221–242.

Williamson, C. (1989):   Oblique and parallel modes of vortex shedding in the wake of a circular cylinder at low Reynolds numbers. *Journal of Fluid Mechanics*, vol. 206, pp. 579–627.

Williamson, C. (1996):   Vortex dynamics in the cylinder wake. *Annual Review of Fluid Mechanics*, vol. 28, pp. 477–539.